Barotropic tidal dynamics in a frictional subsidiary channel

Di Wan, Jody M. Klymak, Michael G.G. Foreman, Stephen F. Cross

2015

Continental Shelf Research 105 (2015) 101–111

Contents lists available at ScienceDirect

Continental Shelf Research

journal homepage: www.elsevier.com/locate/csr

Barotropic tidal dynamics in a frictional subsidiary channel

Di Wan [a,b,c,*], Jody M. Klymak [a,b], Michael G.G. Foreman [c], Stephen F. Cross [d,e]

[a] School of Earth and Ocean Sciences, University of Victoria, Victoria, BC, Canada V8P 5C2
[b] Department of Physics and Astronomy, University of Victoria, Victoria, BC, Canada V8P 5C2
[c] Institute of Ocean Sciences, Fisheries and Oceans Canada, P.O. Box 6000, Sidney, BC, Canada V8L 4B2
[d] Department of Geography, University of Victoria, Victoria, BC, Canada V8P 5C2
[e] SEA Vision Group Inc., Courtenay, BC, Canada V9N 9N8

ARTICLE INFO

Article history:
Received 5 December 2014
Received in revised form
21 May 2015
Accepted 22 May 2015
Available online 29 May 2015

Keywords:
Subsidiary channel dynamics
Numerical modeling
Viscous parameterization
Horizontal eddy viscosity coefficient
Energy flux
Energy dissipation

ABSTRACT

Barotropic M_2 tidal dynamics are studied in a subsidiary tidal channel in Kyuquot Sound, Canada, a site proposed for multi-trophic aquaculture. A regional model with no stratification or forcing other than the tide found that the sea level in the subsidiary channel responded in phase with the rest of Kyuquot Sound, but that the velocity response was almost 180° out of phase. Further, this velocity difference was strongly dependent on the choice of viscous parameterization in the model. A simple linear analytical model was developed to explain the simulated changes in terms of the phase lag induced by viscosity, and allowed a larger parameter regime to be explored. These results suggest that verifying models of smaller channels using sea level measurements alone is inadequate, and velocity measurements are necessary.

1. Introduction

Kyuquot Sound (see Fig. 1) is located on the northwestern coast of Vancouver Island. It supports a number of aquaculture facilities and is home to natural populations of salmon and sablefish as part of their coastal-offshore life cycles. This study was motivated by the development and pre-commercial scale testing of a Sustainable Ecological Aquaculture (SEA), or Integrated Multi-Trophic Aquaculture (IMTA), site located in the northwest region of Kyuquot Sound (SEA Vision Group; see Fig. 1). Combining species from different trophic levels, a SEA/IMTA system is designed to intercept and extract both inorganic and organic wastes. In our case, scallops, oysters, sea cucumbers, and kelp are used to extract wastes generated from the fed culture species, sablefish (Barrington et al., 2009). Operational efficiencies of a SEA/IMTA system can significantly improve from a better understanding of local ocean circulation. In particular, fine resolution circulation models provide hydrodynamic information for the SEA/IMTA site to assist in the assessment and optimization of the system.

Despite the biological importance of the Kyuquot Sound region, the physical oceanography is poorly studied. Union Island is in the middle of Kyuquot Sound, delineating the main Kyuquot Channel from the shallower and narrower Crowther Channel (Fig. 1). The length of the main channel is about 30km, its width is about 2 km, and the average depth is 85 m (ranging from ~10 m to more than ~250 m, Fig. 2). The channels are narrow, so the Coriolis force is neglected in this paper. The tidal flow in this system has not been studied, but the presence of two openings under different tidal forcing, and the potential for high friction in the constrictions of Crowther Channel make predicting the flow at the aquaculture site challenging. Below we show that the friction in the smaller Crowther Channel drives the velocity to be almost 90° out of phase with the elevation forcing.

Flows with friction have been extensively studied theoretically and through field/laboratory experiments and numerical models. The tides can be described as a standing wave in a frictionless rectangular channel (Freeland and Farmer, 1980), where the phase of the currents lags the phase of the elevation by 90°. Hunt (1964), using the Thames River as a case study, pointed out that friction is the cause of phase differences between currents and sea surface elevation in fjord-like channels. When friction is present in a channel, the waves can no longer be considered as a combination of the incoming and the reflective waves with equal amplitude in opposite directions. Energy is lost through friction, so the amplitudes of an incoming and a reflective waves decrease along their propagation directions (Sverdrup, 1942). The difference between the current velocity phase and the elevation phase varies

* Corresponding author at: School of Earth and Ocean Sciences, University of Victoria, Victoria, BC, Canada V8P 5C2.
E-mail addresses: diwan@uvic.ca (D. Wan), jklymak@uvic.ca (J.M. Klymak), Mike.Foreman@dfo-mpo.gc.ca (M.G.G. Foreman), sfcross@uvic.ca (S.F. Cross).

http://dx.doi.org/10.1016/j.csr.2015.05.011

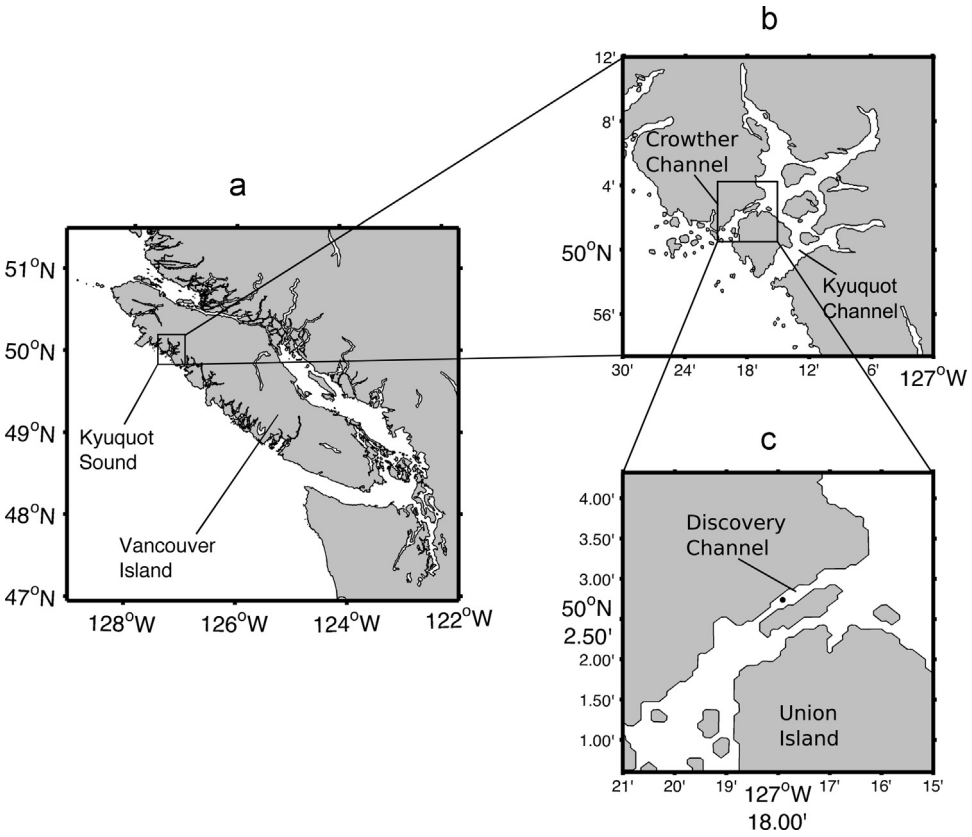

Fig. 1. (a) Vancouver Island. (b) Kyuquot Sound. (c) close-up near the SEA Vision Group farm site (the black dot at 50° 03‵ N, 127°18‵ W). The island between Kyuquot Channel and Crowther channel is Union Island, and henceforth, Crowther Channel will be used to refer to both Crowther and Discovery channels.

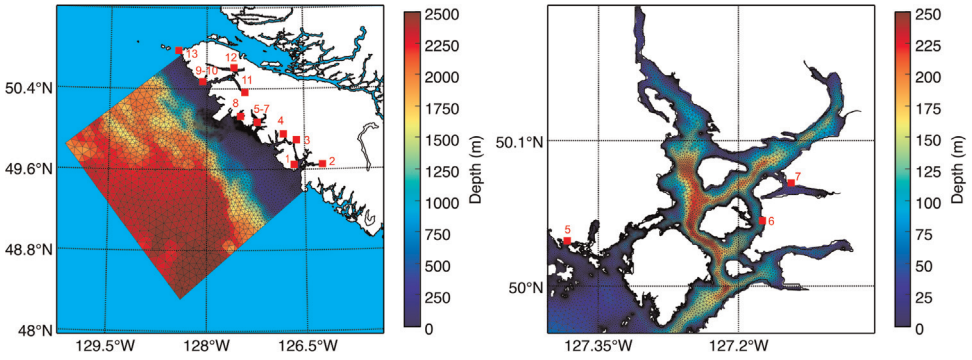

Fig. 2. Bathymetry of the computational domain and the computational grid of Kyuquot Sound. Numbered red dots indicate the locations of 13 tide gauges whose names are listed in Table 1. (For interpretation of the references to color in this figure legend, the reader is referred to the web version of this article.)

continuously along the channel (Freeland and Farmer, 1980). There had been many studies on barotropic energy partitions in fjords (De Young and Pond, 1989; Stacey, 2005), but most only considered the energetics of the fjord's main channel. This paper is focused on the circulation and the energy removal in a subsidiary channel of a fjord system.

This paper examines the barotropic M_2 tidal circulation in Kyuquot Sound and the energy removal in a subsidiary channel (Crowther Channel). Based on numerical results from a Finite-Volume Coastal Ocean Model (FVCOM) application for the region (Section 2), a linear analytical model that describes a two-channel system is developed. This model re-parameterizes the friction as Reynolds drag, and explains the relatively constant elevation phases throughout the main sound. Moreover, it also offers explanations for the difference in velocity phases between a main (Kyuquot) channel and a subsidiary (Crowther) channel, and variations in velocity phase as we move along the subsidiary channel (Section 3). Finally, we utilize the linear model to explain the nonlinear energetic response in the subsidiary channel, test how the velocity in the subsidiary channel changes with the different horizontal viscous parameterizations, and conclude that the velocities are relatively sensitive to these parameterizations (Section 4). The conclusions are summarized in Section 5.

2. Numerical observations

Given the lack of information about Crowther Channel, we have begun a hierarchy of modeling studies, starting with a simple barotropic tidal model that is the focus of this work. The model is the Finite-Volume Coastal Ocean Model (FVCOM) that was developed by Chen et al. (2003, 2006), and uses an unstructured grid to resolve irregular estuarine coastlines. The model is forced with the M_2 tidal elevation and phase specified at open boundaries and is

run without stratification. While numerical approximation considerations are not the main focus of this paper, Chen et al. (2003) have provided detailed descriptions of the model parameters required by FVCOM. Here, we briefly introduce our model setup and then evaluate the accuracy of the barotropic base model through comparisons with observations from thirteen tide gauges and one ADCP current meter. A current phase variation is found along Crowther Channel, while the phase of the elevation remains the same.

2.1. Model setup

A large computational domain (Fig. 2) was chosen so that boundary inaccuracies would be far from the region of interest. The triangular grid has 55,270 unequally spaced nodes, and 98,144 elements. The horizontal resolution varies from 3 km in the open ocean to about 10 m near the aquaculture site (Fig. 2). Vertically, there are 20 non-uniform layers that satisfy a hyperbolic tangent distribution (Pietrzak et al., 2002). The irregular triangular grid was generated primarily by Trigrid (Henry and Walters, 1993).

The computational model bathymetry (Fig. 2) was taken from the Canadian Hydrographic Service single-beam observations and digital charts. The vertical σ-coordinates that FVCOM uses are beneficial when dealing with irregular variable bottom topography (Mellor and Blumberg, 1985), but problems can emerge with steep bathymetry and baroclinic applications. Although the subsequent presentation is focused on barotropic conditions, a bathymetric smoothing method based on a volume preserving technique (Foreman et al., 2012) was employed to avoid these problems with subsequent baroclinic applications.

2.1.1. Initial conditions and boundary forcing

The barotropic model is started from rest and forced at the lateral open boundaries with M_2 tidal elevations prescribed by amplitudes and phases that are interpolated from Foreman et al. (2000). Salinity and temperature are set to constant values and there is no wind or freshwater forcing.

The surface boundary stress is zero, and the bottom boundary condition is defined as:

$$(\tau_{bx},\ \tau_{by}) = C_d \sqrt{u_b^2 + v_b^2}\ (u_b,\ v_b), \tag{1}$$

where C_d=0.0025 is a user-defined frictional coefficient, $(u_b,\ v_b)$ is the velocity vector in the bottom layer.

2.1.2. Turbulence considerations

The Mellor and Yamada (1982) level-2.5 turbulent closure scheme (MY2.5) is used for the vertical eddy viscosity parameterization, and the Smagorinsky horizontal closure scheme (Smagorinsky, 1963) and constant coefficient methods are used for horizontal eddy viscosity terms. In coastal oceans, the horizontal eddy viscosity coefficient (A_m) typically ranges from 0.2 m^2/s to 100 m^2/s (Denniss and Middleton, 1994). In the base run (r_{20}), a value of A_m=20 m^2/s is used as the constant horizontal eddy coefficient as it produces velocities comparable to those observed in the region of interest (see Section 2.2.1). The probable reason for this relatively large A_m is that the main energy loss from the rapidly changing channel width in the subsidiary channel [(c) in Fig. 1] causes more turbulence at subgrid scales. To resolve the subgrid scale processes, a higher viscosity is needed. Two other model runs, which are introduced later in this paper, are conducted using Smagorinsky parameterizations in order to study the sensitivity to the magnitude of the lateral mixing parameters. In the Smagorinsky parameterization scheme, the horizontal diffusion for momentum is given as:

$$A_m = 0.5\ C\ \Omega^u \sqrt{\left(\frac{\partial u}{\partial x}\right)^2 + 0.5\left(\frac{\partial v}{\partial x} + \frac{\partial u}{\partial y}\right)^2 + \left(\frac{\partial v}{\partial y}\right)^2}, \tag{2}$$

where C is a user defined constant parameter, and Ω^u is the area of an individual element. So A_m varies with element sizes and velocities throughout the computational domain. The particular Smagorinsky C values used in other runs are 5.0 (r_{21}), which produces a comparable A_m in Kyuquot Sound as the base run (r_{20}), and 1.0 (r_{23}), which is arbitrarily decreased by a factor of 5 from r_{21} to explore in the parameter space. The results will be discussed in Section 4.

2.2. Barotropic base model results of Kyuquot Sound

The response of Kyuquot Sound to barotropic tidal forcing is examined in this section. Special attention is given to Kyuquot Channel and Crowther Channel where different current features imply different hydrodynamics. The currents behave as standing waves in the Kyuquot Channel (the main channel); an along-channel velocity phase variation is found in the Crowther Channel (the subsidiary channel), and the currents in the channel present a combination of standing wave and progressive wave features.

2.2.1. Model validation

A first check of the model accuracy is provided by examining elevation phases and amplitudes for the major semi-diurnal tidal constituent M_2. There have been 13 tide gauges deployed at various times along the northwest coast of Vancouver Island (Fig. 2), whose tidal records have been harmonically analyzed (Foreman 1977, 1978). The results of this harmonic analysis can be compared against those from our base run r_{20}. As seen in Table 1, except for gauges 11, 12 and 13, the complex distances $[D(\mathrm{cm}) = abs(|\eta_{obs.}|e^{i\theta_{obs}} - |\eta_{mod}|e^{i\theta_{mod}})$, where $\eta_{obs.}$ ($\eta_{mod.}$) and $\theta_{obs.}$ ($\theta_{mod.}$) are the observed (modelled) elevation amplitude and phase, respectively] between observed and modelled results are all less than or equal to 5.0 cm for M_2.

Table 1
M_2 elevation amplitudes (cm) and phases (deg) from 13 tide gauges in the computational domain compared with the harmonic analysis results of a 15-day barotropic base model simulation (r_{20}). D (cm) indicates the distance between the two values (observed and modelled) in complex space.

Stn No.	Name	Time series	Model		Tide gauge		
		Length (days)	Amplitude (cm)	Phase (°, UTC)	Amplitude (cm)	Phase (°, UTC)	D(cm)
M_2:							
1	Saavedra Islands	369	99.0	242.0	99.7	240.0	3.6
2	Gold River	365	101.4	241.9	99.2	240.3	3.5
3	Esperanza	88	99.5	242.2	96.6	240.7	3.9
4	Zeballos	365	99.3	242.3	97.6	241.7	2.0
5	Kyuquot	365	96.7	243.6	99.0	241.4	4.4
6	Copp Island	118	98.2	242.9	98.0	241.0	3.3
7	Fair Harbour	89	96.7	243.2	98.2	241.5	2.9
8	Bunsby Island	59	96.7	243.2	97.5	242.2	1.9
9	Winter Harbour	365	97.5	243.8	100.0	243.5	2.6
10	Hunt Islets	365	97.4	243.8	101.1	243.6	3.7
11	Port Alice	292	106.2	244.0	105.2	248.4	8.2
12	Coal Harbour	358	107.9	244.9	104.8	266.5	40.1
13	Cape Scott	86	101.3	242.2	108.1	244.2	7.7

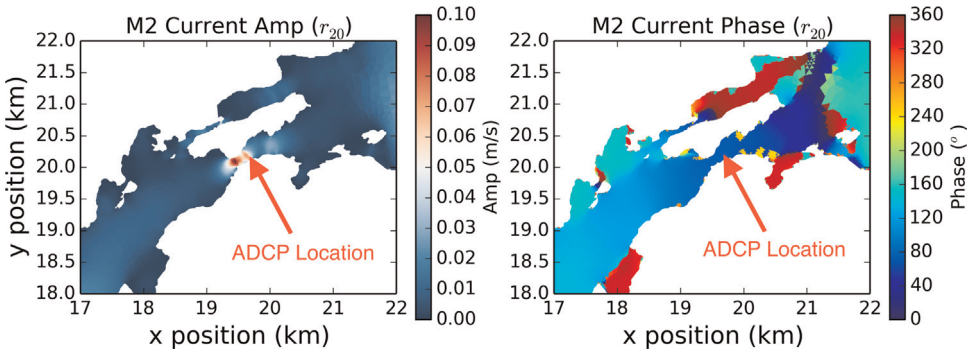

Fig. 3. Crowther Channel ADCP location, and the vertically averaged M_2 amplitude and phase from the numerical model (r_{20}).

This is quite good considering the fact that observed values would include both baroclinic effects and nonlinear interactions from other neglected constituents. The likely reason for the larger discrepancies at gauges 11 and 12 is insufficient spatial resolution, while the larger discrepancy at Cape Scott (gauge 13) is likely due to its proximity to the boundary. Nevertheless, the relatively large discrepancies at these three locations do not affect our location of interest (Kyuquot Sound), where the complex distances (D) are seen to be less than 4.5 cm at gauges 4, 5 and 6.

A short period of ADCP observation data is used to provide some confidence in the model currents. A bottom mounted 1200 kHz ADCP was deployed on Feb 22, 2011 in Crowther Channel, and though it was planned to be recording for 3 months (see Fig. 3 for its location), it was knocked over by the high currents arising from the Japanese Tsunami generated on March 11th, 2011 (the total record length is 17 days). Tidal harmonic analyses of the vertically averaged ADCP currents show essentially rectilinear flows with an M_2 amplitude of 7.0 cm/s, and a phase of 135°. The current amplitude is in agreement with the barotropic base model results (6-8 cm/s; see Fig. 3) in elements near the ADCP location, however, the phase is about 30° (1 h) bigger than the modelled results. As the modelled velocity phase varies over 180° (6 h) from one end to the other of the channel, the 30° discrepancy may simply arise from not accurately choosing the vertical or horizontal eddy viscosity coefficients.

2.2.2. *Tidal current response*

Tides in an enclosed frictionless channel can be most easily understood as standing waves where all the elevations go up and down together and the phase of the current velocity lags the elevation by 90° (Freeland and Farmer, 1980). Harmonic analysis of the model time series shows that M_2 tidal elevations are basically in phase (within 1°) everywhere in Kyuquot Sound with a slightly later phase towards the head of the inlet. The M_2 tidal elevation

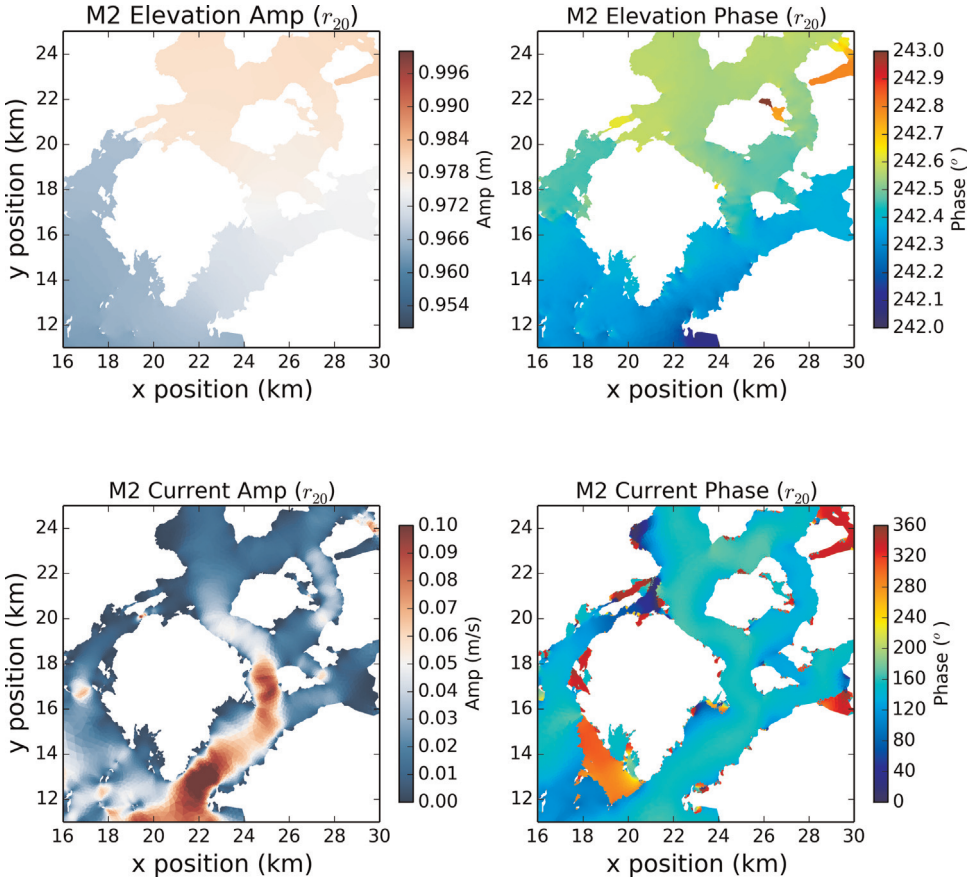

Fig. 4. Sea surface elevation and current velocity phase and amplitude in Kyuquot Sound (r^{20} model results). Note the different color scales used in the top two plots.

amplitude increases by about 1 cm at the head of the inlets, as compared to the mouths, owing to weak tidal resonance (Fig. 4); The M_2 tidal current velocities are also in phase in the Kyuquot Channel (ranging between 150° and 160°, see Fig. 4) and the current velocity phase lags the elevation by approximately 90° (155° versus 242°). This 90° phase lag suggests that the barotropic tide behaves like a standing wave in the Kyuquot Channel, so little energy is lost in the channel.

The barotropic tides are a combination of progressive and standing waves in the subsidiary Crowther Channel. While the elevation phase remains approximately constant (Fig. 4), the tidal current velocity phase decreases from the ocean entrance to the east along Crowther Channel (Fig. 4). This is inconsistent with a standing wave, suggesting that energy is lost in the subsidiary channel.

3. A linear analytical two-channel model

In this section, we formulate a two-channel 1D model, and then use it to compare with and explain the numerical observations.

3.1. Model formulation and assumptions

A two-channel 1D model is proposed to explain the Kyuquot Sound system: a main channel that represents Kyuquot Channel [*AB* in Fig. 5], and a subsidiary channel that represents Crowther Channel [*CO* in Fig. 5(b)]. Points *A* and *C* are the ocean ends of the main and subsidiary channels, respectively; *O* is the join point of the two channels, and *B* is the shore end of the main channel. The approximate average depths of Kyuquot Channel and Crowther Channel are 85 m ($H=85$ m) and 30 m ($h=30$ m), respectively.

The governing equations for the current $u(x, t)$ and the sea surface elevation $\eta(x, t)$ are the linearized 1D continuity equation and the linearized momentum equation:

$$\frac{\partial u}{\partial x} + \frac{1}{H}\frac{\partial \eta}{\partial t} = 0 \tag{3}$$

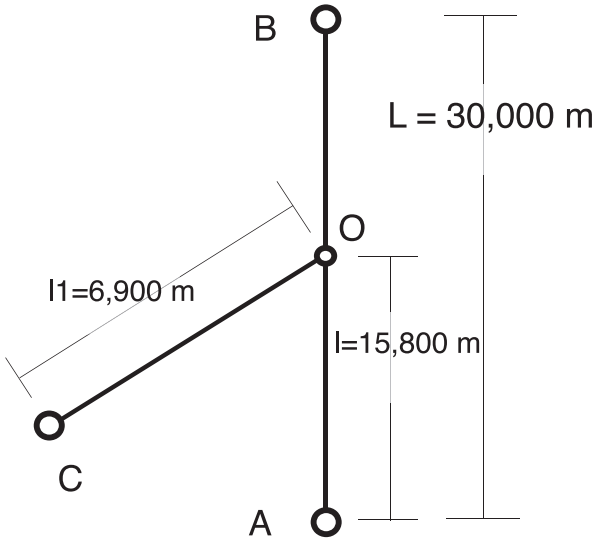

Fig. 5. The two-channel system configuration. AB is the main channel and CO is the subsidiary channel (joining the main channel at point O). The positive current directions are defined from A to B in the main channel, and from C to O in the subsidiary channel. A and C are the ocean mouths. The length dimensions are taken from the actual lengths of the channels.

$$\frac{\partial u}{\partial t} + g\frac{\partial \eta}{\partial x} + \lambda u = 0 \tag{4}$$

where H is the flat bottom depth, g is the gravitational acceleration, and λ is a linear frictional coefficient. It should be noted that the frictional coefficient λ represents all forms of friction, including bottom and horizontal friction.

3.2. Results

3.2.1. Dispersion relation

We assume that solutions for the time and space dependent current velocity (u) and the sea surface elevation (η) are:

$$u = u_o e^{i(\omega t - kx)} \tag{5}$$

$$\eta = \eta_o e^{i(\omega t - kx)} \tag{6}$$

where u_o is the amplitude of the tidal current velocity, η_o is the amplitude of the tidal elevation, ω is the frequency of the M_2 tidal constituent, and k is the wavenumber.

Substituting u and η into the continuity and momentum equations and insisting on a nontrivial solution, we get the following dispersion relationship:

$$k_{\pm} = \pm\, k_r e^{i\phi_k} \tag{7}$$

where $k_r = \sqrt{\frac{\omega}{gH}}\left(\omega^2 + \lambda^2\right)^{\frac{1}{4}}$, and $\phi_k = \frac{1}{2}\tan^{-1}(-\frac{\lambda}{\omega})$. Note that if $\lambda = 0$ (no friction), k is a real number, and the dispersion relation simply becomes the shallow water relationship $k_{\pm}=\pm\frac{\omega}{\sqrt{gH}}$. We define $k=k_+$ for the rest of the paper.

3.2.2. Analytic model solutions

In the main channel, solutions of the time and space dependent sea surface elevation $\eta(x, t)$ and tidal current velocity $u(x, t)$ are assumed to be a combination of incoming and reflected waves:

$$u(x, t) = u_0 e^{i(\omega t - kx)} + u_0' e^{i(\omega t + kx)} \tag{8}$$

$$\eta(x, t) = \eta_0 e^{i(\omega t - kx)} + \eta_0' e^{i(\omega t + kx)} \tag{9}$$

where u_o and u_o' are the amplitudes of the tidal current travelling from A to B and from B to A, respectively; η_o and η_o' are the amplitudes of the tidal elevation travelling from A to B and from B to A, respectively.

Boundary conditions that are prescribed at $A(x = 0)$, and $B(x = L)$ are:

$$u(L, t) = 0 \tag{10}$$

$$\eta(0, t) = \eta_A e^{i\omega t} \tag{11}$$

where η_A is the elevation amplitude at A.

We then obtain the general solutions for $u(x, t)$ and $\eta(x, t)$:

$$u(x, t) = \left(\frac{\omega}{kH}\frac{\eta_A}{e^{-2ikL} + 1}\right) e^{i(\omega t - kx)} + \left(-\frac{\omega}{kH}\frac{\eta_A e^{-2ikL}}{e^{-2ikL} + 1}\right) e^{i(\omega t + kx)} \tag{12}$$

$$\eta(x, t) = \left(\frac{\eta_A}{e^{-2ikL} + 1}\right) e^{i(\omega t - kx)} + \left(\frac{\eta_A e^{-2ikL}}{e^{-2ikL} + 1}\right) e^{i(\omega t + kx)} \tag{13}$$

Given the dimension of the settings and if $\lambda = 0$, we have $kL = 0.14 \ll 1$, then we can approximate the solutions as

$$u(x,\,t) = \eta_A \frac{\omega}{kH}\ \sin(kx)\cos\left(\omega t - \frac{\pi}{2}\right) \tag{14}$$

$$\eta(x,\,t) = \eta_A\ \cos(kx)\cos(\omega t) \tag{15}$$

As λ goes to 0 ($k = k_r$), there is no energy loss in the system, and the current velocity phase lags the elevation by 90° in agreement with the standing wave approximation in a frictionless enclosed channel. Also, when λ increases from 0, an x-dependent phase change arises in η and u.

In the side channel, we assume the same solution format as for the main channel:

$$u_1(x,\,t) = u_{10}e^{i(\omega t - k_1 x)} + u'_{10}e^{i(\omega t + k_1 x)} \tag{16}$$

$$\eta_1(x,\,t) = \eta_{10}e^{i(\omega t - k_1 x)} + \eta'_{10}e^{i(\omega t + k_1 x)} \tag{17}$$

where u_{10} and u'_{10} are the amplitudes of the tidal current travelling from C to O and from O to C, respectively; η_{10} and η'_{10} are the amplitudes of the tidal elevation travelling from C to O and from O to C, respectively. $k_1 = \sqrt{\frac{\omega}{gh}}\ \sqrt{\omega - i\lambda_1}$ is the wave number and λ_1 is the frictional coefficient in the subsidiary channel.

Boundary conditions are defined by the sea surface elevations at two ends of the side channel. The elevation solution at O ($x = l$, where the subsidiary channel joins the main channel) that we obtained from the main channel provides the first boundary condition, and we prescribe the elevation amplitude and phase at the seaward end (C) of the subsidiary channel as our second boundary condition.

$$\eta_1(0,\,t) = \eta_C e^{i(\omega t - \alpha)} \tag{18}$$

$$\eta_1(l,\,t) = \eta(l,\,t) \tag{19}$$

It is shown in Fig. 4 that the sea surface elevation is continuous everywhere in the sound, including at the juncture point O. The second boundary condition (Eq. 19) says that sea surface elevation continuity must be maintained. The subsidiary channel is forced by the elevations at the two ends of the channel and its dynamics do not feed back to the main channel. This approximation is reasonable because the volume flux in the subsidiary channel is only about 3% of the volume flux of the main channel (Fig. 6), as calculated from our numerical base run. This same run shows that the currents in the subsidiary channel enter from the main channel at O and the energy is propagating westward from O to C

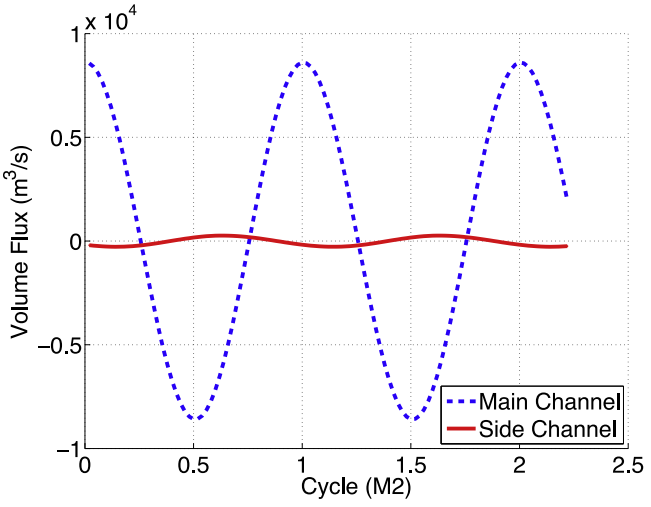

Fig. 6. Volume fluxes in the main and the subsidiary channel taken from transects close to the juncture point O (r_{20}).

while getting dissipated. This energy is a small fraction of the energy in the main channel, and thus can be ignored in our analytical model.

Note that previously in our main channel, we did not give an elevation phase at point A, so effectively the phase α here is the elevation phase difference between the main channel entrance and the subsidiary channel entrance ($\alpha = \alpha_C - \alpha_A$).

The general solutions in the subsidiary channel are then:

$$u_1(x,\,t) = \left(\frac{\omega}{k_1 h} \frac{\frac{\eta_A e^{-ikl}}{e^{-2ikL}+1} + \frac{\eta_A e^{-2ikL}}{e^{-2ikL}+1} e^{ikl} - \eta_C e^{i(kl-\alpha)}}{e^{-ik_1 l_1} - e^{ik_1 l_1}} \right) e^{i(\omega t - k_1 x)}$$
$$- \frac{\omega}{k_1 h} \left(\eta_C e^{-i\alpha} - \frac{\frac{\eta_A e^{-ikl}}{e^{-2ikL}+1} + \frac{\eta_A e^{-2ikL}}{e^{-2ikL}+1} e^{ikl} - \eta_C e^{i(kl-\alpha)}}{e^{-ik_1 l_1} - e^{ik_1 l_1}} \right) e^{i(\omega t + k_1 x)} \tag{20}$$

$$\eta_1(x,\,t) = \left(\frac{\frac{\eta_A e^{-ikl}}{e^{-2ikL}+1} + \frac{\eta_A e^{-2ikL}}{e^{-2ikL}+1} e^{ikl} - \eta_C e^{i(kl-\alpha)}}{e^{-ik_1 l_1} - e^{ik_1 l_1}} \right) e^{i(\omega t - k_1 x)}$$
$$- \left(\eta_C e^{-i\alpha} - \frac{\frac{\eta_A e^{-ikl}}{e^{-2ikL}+1} + \frac{\eta_A e^{-2ikL}}{e^{-2ikL}+1} e^{ikl} - \eta_C e^{i(kl-\alpha)}}{e^{-ik_1 l_1} - e^{ik_1 l_1}} \right) e^{i(\omega t + k_1 x)} \tag{21}$$

Following the same simplification and approximation method as in the main channel (namely L and l are much smaller than the M_2 wavelength), and applying the pre-defined dimensions in the Kyuquot model setup, we have:

$$u_1(x,\,t) = \frac{\eta_A + \eta_C e^{-i\alpha}}{2} \frac{\omega}{k_1 h}\ \sin(k_1 x)\cos\left(\omega t - \frac{\pi}{2}\right) \tag{22}$$

$$\eta_1(x,\,t) = \frac{\eta_A + \eta_C e^{-i\alpha}}{2}\ \cos(k_1 x)\cos(\omega t) \tag{23}$$

Similarly to the main channel, increasing the frictional coefficient from 0 will cause an x-dependent phase shift in u_1 and η_1, and the elevation phase difference and amplitude difference will also affect the phases in u_1 and η_1. In fact, increasing λ_1 is effectively making k_1 complex, so the imaginary component of k_1 provides a more significant x-dependent effect in u_1 through $\sin(k_1 x)$, and has a much less effect in η_1. Therefore, if the frictional coefficient is high (e.g., in the subsidiary channel), we may not see a large phase shift in η_1, but the along-channel phase change in u_1 could be substantial.

3.3. Frictional effects

The effective linear frictional coefficient λ_1 in the subsidiary channel can be determined by measuring the velocity phase difference along-channel. When an inlet is frictional, kinetic energy will be lost through frictional processes and cause along-channel phase variations (Sverdrup, 1942). As discussed previously, given our dimensions and assumptions, the frictional process affects the velocity's phase more significantly. In this section, we explain how the frictional coefficient λ_1 is determined.

The velocity phase difference between two transects (at $x = 2600$ m and $x = 6600$ m in Fig. 7) increases as we increase the frictional coefficient λ_1 in the subsidiary channel of our linear model (see Fig. 8). A few variables are needed to determine the velocity in the subsidiary channel, specifically η_A, η_C, α, k, and k_1 (in u_1 and η_1 solutions). η_A, η_C [elevation amplitudes at the Kyuquot Channel ($\eta_A = 0.9687$ m) and the Crowther Channel ($\eta_C = 0.9675$ m) ocean entrances, respectively] and α (elevation phase difference $\alpha = \alpha_C - \alpha_A = 43.89^\circ - 43.73^\circ$) are taken from

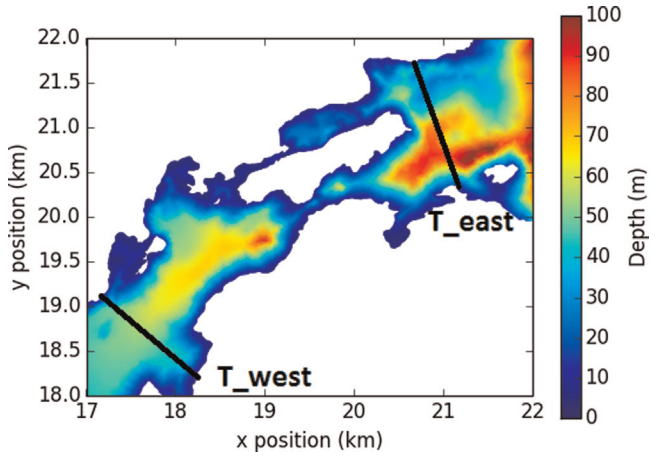

Fig. 7. Crowther Channel and the locations of T_west ($x = 2600$ m) and T_east ($x = 6600$ m).

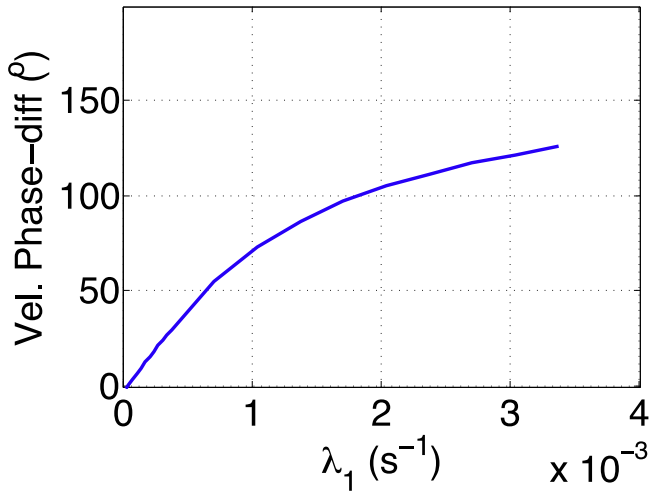

Fig. 8. M_2 velocity phase-difference from T_west to T_east in the linear analytical model as λ_1 increases.

harmonically analyzed results from the base model run; assuming the friction is negligible in the main channel (setting the frictional coefficient $\lambda = 0$), the wavenumber k is obtained; k_1 can be calculated for a given λ_1.

It should be noted that the phase difference is not exactly 0 when $\lambda_1 = 0$. This is because we have only prescribed the elevation at two ends of the subsidiary channel, and thus we effectively allow for a current velocity separation at the join point.

We can now determine λ_1 by matching the phase difference in the model to the curve in Fig. 8. In the numerical model base run, it is shown that the velocity phase increases from T_east ($x = 6600$ m) to T_west ($x = 2600$ m) by approximately 100° (T_west and T_east are marked in Fig. 7), suggesting energy enters Crowther Channel from the east end and dissipates in the channel. This 100° phase difference corresponds to $\lambda_1 = 0.0018\ s^{-1}$. The linear drag coefficient λ_1 in our 1-D linear model represents all forms of energy losses, in this case also including the strong lateral dissipation.

The linear model predicts a phase drop in the along-channel distance and is in good agreement with the numerical simulation (Fig. 9). There is a bias of about 20°, likely caused by small inaccuracies in estimating the elevation at the join point (O). An η parameter space exploration shows that the solutions in the channel are very sensitive to the η values prescribed at both ends of a channel, as will be seen in the next section.

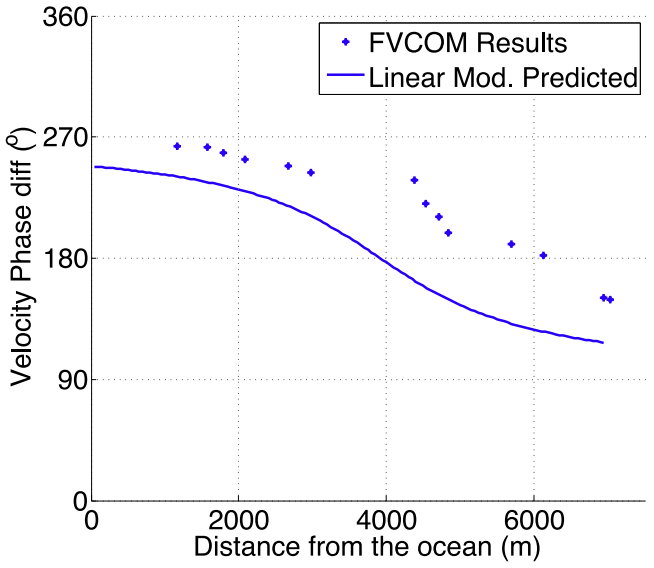

Fig. 9. Velocity phase along Crowther Channel (subsidiary channel) for the numerical model and linear analytical model.

4. Sensitivity to viscous parameterization

The dynamics of the subsidiary channel are relatively sensitive to the choice of viscous parameterization. We explore this here by running the numerical simulation with different lateral viscosities, and by exploring the sensitivity in the analytical model. Increasing the lateral viscosity decreases the dissipation in both the simulation and analytical models because the velocity in the subsidiary channel is strongly dependent on the dissipation in the channel. We also test if slight changes in forcing caused by changes in the rest of the system (i.e., beyond Kyuquot Sound) could cause the changed velocities, and find that although this could be a major effect, it is not dominant in our system.

4.1. Subsidiary channel energetics in three numerical runs

We first carry out three numerical simulations with different horizontal eddy viscosity parameterizations (Table 2), and find

Table 2
Differences in 3 numerical simulations and energy budget results. See Eqn. (2) for the expression for C=5.0 (r_{21}) provides a generally smaller A_m in Crowther Channel than what is used in r_{20}. The near zero energy terms are calculated for a section of the subsidiary channel (from T_west to T_east, see Fig. 7) from the last tidal cycle of each of the simulations. The near 0 energy tendencies (dE/dt) indicate that all three runs have reached a steady state.

Horizontal viscosity	r_{20}	r_{21}	r_{23}
Constant A_m (m^2/s)	20.0		
Smagorinsky C		5.0	1.0
Energy terms	[kW]	[kW]	[kW]
dE/dt	−0.000	-0.038	0.000
Energy Flux (T_west)	−857.564	−3828.620	−4524.798
Energy Flux (T_east)	−866.983	−3871.851	−4583.148
∇· Flux	−9.419	−43.231	−58.350
Advection	−0.001	4.037	9.122
Dissipation (D)	9.420	39.232	49.228
Vert. dissipation	0.014	0.370	0.627
Hor. dissipation	11.096	45.819	24.659
Explicit dissipation (ED)	11.110	46.189	25.286
$\lvert D - ED\rvert/D$	18%	18%	−49%

that when the horizontal eddy viscosity coefficient is reduced, the dissipation in the subsidiary channel increases. T_west and T_east are the cross-sections of the subsidiary channel, as shown in Fig. 7. Along with the coast lines, T_west and T_east cross-sections form a volume-confined 'box', and energy partitions are calculated within the 'box'. Also note that the T_west to T_east is the middle part of the subsidiary channel. The distance between T_west and T_east is 4000 m, and the length of the subsidiary channel is 6900 m.

Following the energy budget analysis of (Carter et al., 2008), the vertically averaged energy density equation has the terms:

$$\begin{aligned}
&\text{Tendency}\left(\frac{dE}{\rho dt}\right):\ h\frac{\partial}{\partial t}\frac{\left(\bar{u}^2+\bar{v}^2\right)}{2}+\frac{\partial}{\partial t}\left(\frac{g\eta^2}{2}\right)\\
&\nabla\cdot\text{Flux}:\ \frac{\partial}{\partial x}(h\bar{u}g\eta)+\frac{\partial}{\partial y}(h\bar{v}g\eta):\\
&\text{Advection}:\ h\bar{u}\bar{A}_x^{'}+h\bar{v}\bar{A}_y^{'}\\
&\text{Explicit Dissipation(ED)}:\\
&-\left[h\bar{u}\left(\bar{D}_x+\bar{F}_x\right)+h\bar{v}\left(\bar{D}_y+\bar{F}_y\right)\right]\\
&\text{Dissipation}(D):-\left(\frac{dE}{\rho dt}+\nabla\cdot\text{Flux}+\text{Advection}\right)
\end{aligned}\tag{24}$$

The horizontal bar denotes a tidally averaged quantity, $\left(D_x,\ D_y\right)$ and $(F_x,\ F_y)$ are the vertical and horizontal dissipative terms, and $\left(A'_x,\ A'_y\right)$ is the advection [see Carter et al. (2008) for details]. We define the combination of vertical dissipation and horizontal dissipation as the Explicit Dissipation (ED), which is all the dissipation that we can explicitly account for. If the numerical simulation has reached a steady state, the first term (tendency) should be 0. Also, the ED term should be comparable to the Dissipation term calculated from the residual energy divergence if numerical dissipation is small. We have neglected the baroclinic energy term because there is no stratification. However, the velocities are not completely constant with depth because of boundary layer friction, so this is only an approximation. We check this approximation by comparing the total kinetic energy to the kinetic energy calculated from the depth-mean, and find at most a 15% difference, which is smaller than other uncertainties.

There are a few points in the energy budget results (Table 2) worth addressing. First, the horizontal dissipation dominates the explicit dissipation (ED) in each run. Second, there are some disagreements between the Dissipation (D) and Explicit Dissipation (ED) terms, likely due to increased numerical dissipation as the eddy viscosity is decreased. Last, the increasing energy flux at T_west/T_east with decreasing horizontal eddy viscosity coefficient is caused by the increased velocities.

Most interestingly, the decreased viscosity leads to an increased dissipation due to the increased velocities admitted in the channel. There are two possible causes for the increased velocities, which we consider below. The first is that changing the lateral viscosity changes the large-scale system, and hence the boundary conditions change, i.e. the sea-surface elevation at either side of the channel has different amplitudes and/or phases. The second possibility is that the increased velocity is simply due to the reduced viscosity inside the channel.

The analytical model is a good tool to answer these questions, but first we determine if it is able to reproduce the observed changes in dissipation. We follow these steps to reproduce the dissipation with our linear model (all the values mentioned below are listed in Table 3): First we compute η_A, η_C (elevation amplitude at A and C) and α (elevation phase difference between A and C) from each of the numerical simulations and use that to force the analytical model. We then vary the friction coefficient in the analytical model (λ_1) until the appropriate phase drop between T_west and T_east is found and use that as the Reynolds drag in the analytical model. We then compare the average dissipation per unit surface area in the analytical model $\left(\frac{1}{dx}\int_{x_1}^{x_2}\lambda_1 u_1^2 h\,dx,\ x_1=2600\text{ m},\ x_2=6600\text{ m}\right)$ averaged over one tidal cycle and compare to the dissipation per unit surface area from each simulation by dividing the Dissipation (D) terms by the associated area (4.6×10^6 m^2) between T_west and T_east.

Table 3
Unit area dissipation results and the input variables (numerical model v.s. prediction of linear model). Velocity phase diff is the velocity phase difference between T_west and T_east, η_A and η_c are the M_2 elevation amplitudes at A and C, respectively, and α is the M_2 elevation phase difference at A and C.

		r_{20}	r_{21}	r_{23}
Input variables	Velocity phase diff. ϕ(°)	100	20	30
	η_A (m)	0.9687	0.9679	0.9679
	η_c (m)	0.9675	0.9671	0.9671
	$\alpha=\alpha_c-\alpha_A$ (°)	0.1636	0.1264	0.1307
Associated λ_1 $\left(s^{-1}\right)$ in the linear model		0.00180	0.00021	0.00033
Unit Area Dissipation Rate (W/m^2)	modelled	0.0020	0.0085	0.0107
	predicted	0.0024	0.0071	0.0058
Velocity amplitude @ T_west (m/s)	modelled	0.0084	0.0175	0.0221
	predicted	0.0095	0.0516	0.0363

The averaged dissipation rates predicted by the analytic model are in good agreement with the ones calculated from the numerical model (up to 80%; Table 3) for r_{20} and r_{21}, but in poorer agreement for r_{23} (factor of 2). The poorer agreement for r_{23} is likely caused by numerical dissipation.

The velocity amplitude at T_west predicted by the linear model agrees well with the higher friction coefficient case (r_{20}), but poorly for those two cases with lower friction coefficients (r_{21} and r_{23}). Moreover, the velocity amplitude at T_west increases significantly (doubled from r_{20} to r_{21}) as the friction coefficient decreases. The poorer agreements in velocities are likely due to the relatively high sensitivity to the friction in the low friction cases, as will be discussed below.

Note that the boundary forcing η_A and η_c are almost the same between the runs, within less than 1 mm in amplitude and have a very small phase difference. Furthermore, although not shown here, the rms (root mean square) of the cross-sectional energy flux in the main channel only varied within 1% of each other during the three runs, but the rms fluxes within the subsidiary channel increased 5 and 6 times (r_{21} and r_{23}, respectively), relative to that for r_{20}. The fact that the boundary forcing η_A and η_C are almost identical in these three runs, as well as the fact that the main channel dynamics have hardly changed, suggests that the overall dynamics are unlikely to be the cause of the large dissipation differences of the three runs in the subsidiary channel. However, now that we have some confidence in the analytical model we can test this boundary forcing sensitivity easily.

4.2. Uncertainty quantification

Here we show that a relatively large difference in the complex amplitude forcing between A and C is needed to significantly alter the dissipation in the channel. The required differences are small compared to the different forcing in the numerical simulations, but they are not small relative to observational capabilities, and therefore conclusions drawn from pressure gauge records should be treated with care.

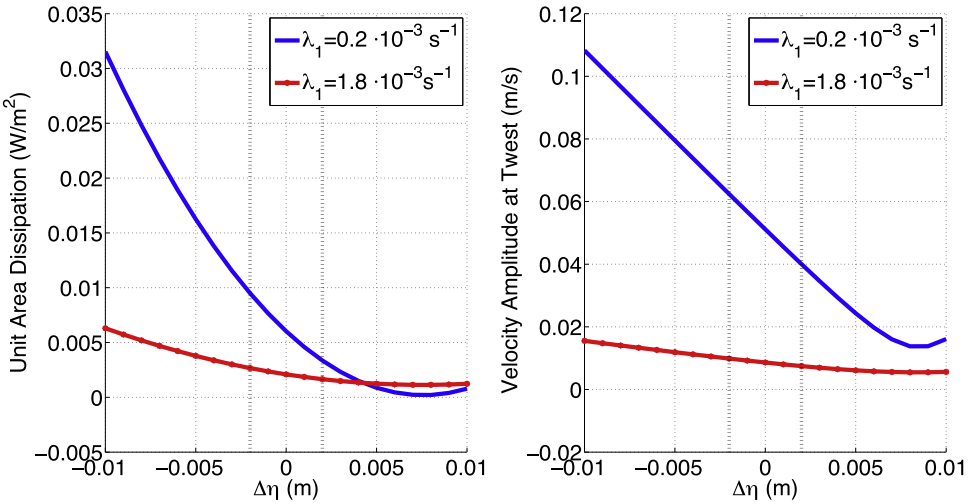

Fig. 10. Dissipation and velocity variations with different $\Delta\eta$. Two scenarios are plotted here: i) the low friction coefficient case ($\lambda_1 = 0.2 \times 10^{-3}$ s^{-1}), which is associated with r_{21} and r_{23}, and ii) the medium-high friction ($\lambda_1 = 1.8 \times 10^{-3}$ s^{-1}), which is associated with r_{20}. The unit area dissipation and the velocity are evaluated for each η_C ($0.9675\ m \pm \Delta\eta$) in both the low and high friction coefficient cases. Also note that the dissipation and the velocity curves are symmetric around $\Delta\eta = 0.008$ m, at which $\Delta\eta$ the elevation amplitudes at C and O (the two ends of the subsidiary channel) are the same (0.9687 m), and therefore the dynamic response is symmetric around that point.

4.2.1. $\Delta\eta$ Sensitivity test

We conduct the sensitivity study by assuming $\alpha = 0$ (no elevation phase difference between A and C), $\eta_A = 0.9687$ m (same as in r_{20}), and $\eta_C = 0.9675\ m \pm \Delta\eta$ (same η_C in r_{20} with uncertainty $\Delta\eta$) to examine the sensitivity of the dissipation and the velocity to $\Delta\eta$. We test this with a low and high value of $\lambda_1 = 0.2 \times 10^{-3}$ s^{-1} and 1.8×10^{-3} s^{-1}, respectively. In the low-friction case (blue line in Fig. 10), a ±2 mm difference (indicated by the black vertical dashed lines) in $\Delta\eta$ could result in a 50% difference in dissipation (0.0080 ± 0.0040 W/m^2), and a 20% difference in velocity (0.056 ± 0.012 m/s). Conversely, in the high frictional coefficient case (red line in Fig. 10), a ±2 mm difference in $\Delta\eta$ only corresponds to a 20% uncertainty in dissipation (0.0028 ± 0.0006 W/m^2), and 10% in velocity (0.009 ± 0.001 m/s).

4.2.2. $\Delta\phi$ Sensitivity test

A phase difference in the forcing between A and C, ϕ, can also change the dissipation and velocities in the channel. The linear model estimated quantities have 20–30% uncertainties in relation to a 10° difference in ϕ in the low λ_1 case (Fig. 11), as compared to those of the high λ_1 case (0–20%). Imposing a 10° difference in ϕ with r_{20} elevation boundary conditions and subsequently finding λ_1 with uncertainties, the unit area dissipation and velocities along with their uncertainties are evaluated for each λ_1 in both low ($\phi = 25°$, red line in Fig. 11) and high ($\phi = 100°$, blue line in Fig. 11) frictional coefficient cases. It is clearly shown that in Table 4 with $\Delta\phi = 10°$, the uncertainties in the low frictional coefficient case are generally 10% larger than the high-friction case.

Table 4
Uncertainties in the linear model predicted unit area dissipation and the velocity, in relation to a 10° error in ϕ (the velocity phase-difference).

Vel. Phase-diff $\phi \pm \Delta\phi$(°)	100 ± 10	25 ± 10
λ_1 (s^{-1})	0.0019 ± 0.0004 (20%)	0.0003 ± 0.0001 (33%)
Unit area dissipation (W/m^2)	0.0024 ± 0.0001 (4%)	0.0067 ± 0.0014 (21%)
Velocity @ T_west (m/s)	0.0095 ± 0.0016 (17%)	0.046 ± 0.013 (28%)

4.3. Sensitivity to viscosity

From the linear model, we saw that both the elevation boundary forcing and the drag coefficient can change the dynamics in the subsidiary channel. However, given the relatively small range of the elevation boundary forcing in the three simulations, the increased dissipation we found in the numerical simulations is caused by the different drag coefficients.

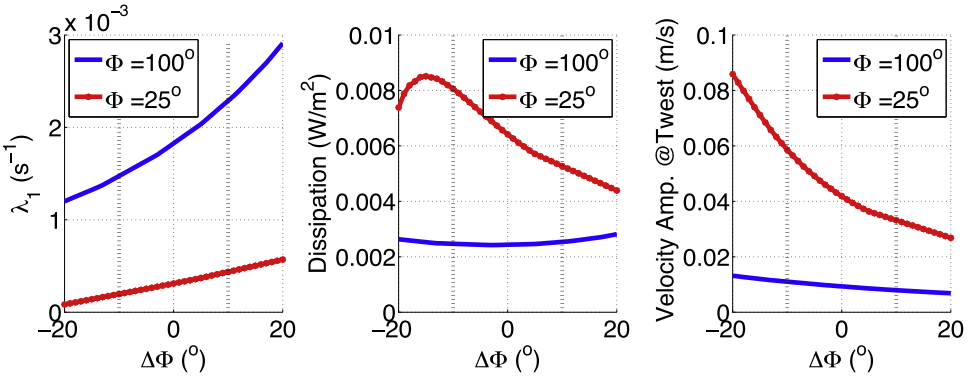

Fig. 11. Variations in the linear model estimated frictional coefficient λ_1, unit area dissipation, and the velocity amplitude with different $\Delta\phi$. Two cases are plotted here: i) the high frictional coefficient case $\phi = 100°$[blue (darker) line] and ii) the low frictional coefficient case $\phi = 25°$[red (lighter) line]. The black dashed lines indicate how much uncertainty in each of the estimators we expect in relation to a ±10° error in ϕ. (For interpretation of the references to color in this figure legend, the reader is referred to the web version of this article.)

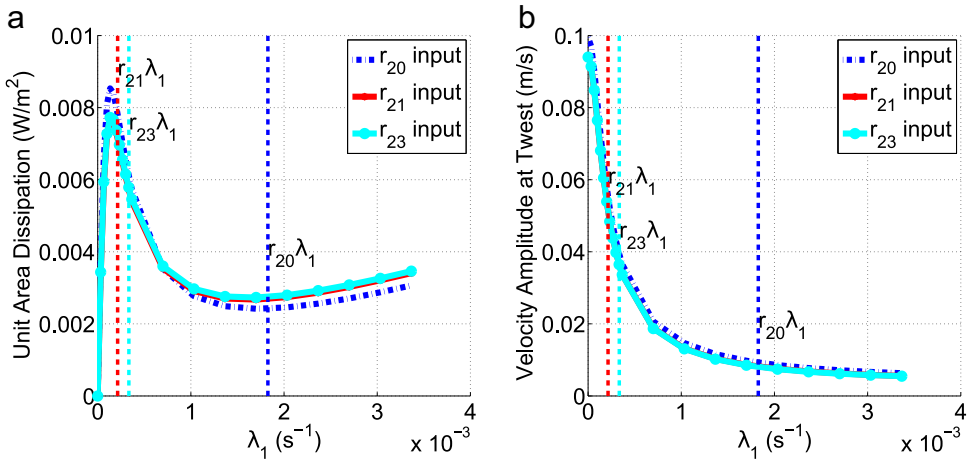

Fig. 12. Variations in (a) unit area dissipation and (b) velocity amplitude at T_west with different drag coefficients. Three different lines in each plot are generated by solutions evaluated by different η_A, η_C and α values from each simulation. The corresponding drag coefficients that are calculated from the model results are also labeled on both plots with vertical dashed lines.

The dissipation and velocity responses vary non-linearly with friction. For low-frictions ($\lambda_1 < 1 \times 10^{-3}$ s^{-1}), the dissipation first increases and then decreases rapidly, as λ_1 increases from 0. For higher frictions, the dissipation curve is relatively flat and goes up slightly after $\lambda_1 = 1.8 \times 10^{-3}$ s^{-1}, suggesting the dissipation is less sensitive to the change of λ_1 within this range (Fig. 12). Velocity amplitude decreases monotonically with increasing λ_1, and the slope of the velocity is bigger in the low friction region ($\lambda_1 < 1 \times 10^{-3}$ s^{-1}), as compared to higher friction region.

Above, we saw that the velocity amplitude in r_{21} and r_{23} were not well-explained by the analytical model. This is partially caused by the sharp change in the velocity response at low friction (Fig. 12b) leading to uncertainties in the estimate of λ_1, and it is also likely caused by the non-linear viscosity in the simulations.

We tested a range of boundary conditions in the simulations (η_A, η_C, and α in Table 3) using the analytical model, and all three curves are almost on top of each other (Fig. 12). This indicates that these small differences in the elevation boundary conditions are not big enough to change the velocity or dissipation response as a function of λ_1 in the subsidiary channel.

It should also be noted that although these studies are focused on the M_2 tidal constituent, at the Crowther Channel mooring (Fig. 3), the diurnal components are important, though not dominant (the along-channel K_1 component amplitude is 6.0 cm/s versus 7.8 cm/s for M_2). Given K_1's lower frequency (longer wavelength), we expect a smaller pressure gradient between the two ends of the subsidiary channel, and therefore, similar but smaller velocity and dissipation responses.

5. Summary

We have examined the barotropic M_2 tidal circulation and its associated dissipation mechanisms in Kyuquot Sound, located off northwestern Vancouver Island, Canada. The circulation pattern presented in the numerical simulation shows different velocity phases in Crowther Channel (the subsidiary channel) from Kyuquot Channel (the main channel). Frictional processes in the subsidiary channel are found to be responsible for the velocity along-channel phase variation.

A linear analytical 1D model has been formulated to describe a two-channel system (i.e. one main channel, and one subsidiary channel), and its predicted unit area dissipation agrees well with the FVCOM model results, while the velocity estimates have larger discrepancies when the friction is low. When the friction is low, the velocity is very sensitive to changes in the frictional coefficient. This is probably why we have poorer velocity agreement in the low friction cases, although it is also likely caused by the non-linear nature of the simulated viscosity.

One outstanding problem is balancing the energy budget in the subsidiary channel. It is clear that the energy budgets presented in Table 2 do not balance very well, especially for r_{23}. The kinetic energy equation is a consequence of the momentum equations, so the discretized kinetic energy equation should be a consequence of the discretized momentum equations. Because the kinetic energy equation and the momentum equation are not independently formed, it is not possible to enforce kinetic energy conservation, while enforcing momentum conservation in a finite-volume numerical method (Ferziger and Peric, 2002).

Therefore, it should not be a surprise to have a poorer energy balance when we have a more energetic system (r_{23}). It may also be necessary to re-formulate the energy budget equation to include the energy in deviations from depth-averaged quantities. This might provide a better understanding of energy conservation in the subsidiary channel and provide a better or more sensible agreement with the linear analytical model. Nevertheless, this should not change our primary findings.

The sensitivity of the velocity in the subsidiary channel to numerical friction is troubling for tuning numerical models of shallow channels. Though these models are routinely ground-truthed against tide gauge observations, our results show these can be in agreement, but the velocities can vary significantly. Hence if tidal currents are a goal of the modeling effort, there is significant value to collecting current meter records to assess the performance of the model.

The numerical and the analytical results discussed in this paper are focused on the unstratified flow, so another potentially important source of friction that has not been studied is the internal wave drag due to stratified flow over the rough sea-floor topography. This will be the focus of future work, but it seems unlikely that the overall conclusion about the sensitivity of the subsidiary channel to friction will change. Rather the sources of the friction will be more complicated. Given the dominance of lateral stresses and the relatively shallow water column in Crowther Channel, we suspect the barotropic forcing is capturing the lowest order physics.

How the circulation responds to a combination of tidal constituents in baroclinic conditions (with temporal and spatially varying temperature, salinity, and density fields) is yet to be investigated. Most importantly, if we use the linear analytical model

to predict and describe the real current circulation for navigation and aquaculture purposes, it needs to have the ability to deal with stratified flow and wind stress. Furthermore, we would like to see if the linear analytical model is sufficiently general to be used in other geographically similar locations (i.e., a primary and a secondary channel share a non-seaside point), such as Puget Sound, Strait of Georgia and Juan de Fuca Strait. These results can be tested either against more numerical models, or field observations.

This work has important implications to the development of new forms of aquaculture, especially those (such as SEA/IMTA designs) that will rely largely on the ability to delimit flow regime in and around production facilities. These regional models will provide valuable support for coastal zone planning (carrying capacity of aquaculture) as well as for site-specific design and engineering work that will continue to improve operational efficiencies and organic/inorganic waste mitigation.

Acknowledgments

We would like to thank the Canadian Integrated Multi-Trophic Aquaculture Network (CIMTAN) for providing the funding and multi-disciplinary communication opportunities for this study, Darren Tuele for deploying and recovering the ADCP in Crowther Channel, and the Centre for Ocean Model Development for Applications (COMDA) within the Department of Fisheries and Oceans Canada (DFO) for providing the multi-processor clusters on which the models were run. We would also like to thank Charles Hannah for his valuable comments.

References

Barrington, K., Chopin, T., Robinson, S., 2009. Integrated Mariculture: A Global Review. In: Soto, D. (Ed.), FAO Fisheries and Aquaculture Technical Paper, 529 p.

Carter, G.S., et al., 2008. Energetics of M2 Barotropic-to-Baroclinic Tidal Conversion at the Hawaiian Islands. J. Phys. Oceanogr. **38**, 2205–2222.

Chen, C., Liu, H., Beardsley, R.C., 2003. An unstructured grid, finite-volume, three-dimensional, primitive equations ocean model: application to coastal ocean and estuaries. J. Atmos. Ocean. Technol. **20**, 159–186.

Chen, C., Beardsley, R.R.C., Cowles, G.G.W, 2006. An Unstructured Grid, Finite-Volume Coastal Ocean Model FVCOM User Manual, 315.

Denniss, T., Middleton, J.H., 1994. Effects of viscosity and bottom friction on recirculating flows. J. Geophys. Res. **99**, 10183. http://dx.doi.org/10.1029/93JC03588.

Ferziger, J.H., Peric, M., 2002. Computational Methods for Fluid Dynamics, 3rd ed. Springer.

Foreman, M.G.G., 1977. Manual for tidal heights analysis and prediction. Institute of Ocean Sciences, Patricia Bay, Sidney, BC, p. p. 97, Pacific Marine Science Report 77-10.

Foreman, M.G.G., 1978. Manual for tidal currents analysis and prediction. Institute of Ocean Sciences, Patricia Bay, Sidney, BC, p. p. 57, Pacific Marine Science Report 78-6.

Foreman, M.G.G., Crawford, W.R., Cherniawsky, J.Y., Henry, R.F., Tarbotton, M.R., 2000. A high-resolution assimilating Tidal Model for the northeast Pacific Ocean. J. Geophys. Res. **105**, 629–651.

Foreman, M.G.G., Stucchi, D.J., Garver, K.A., Tuele, D., Isaac, J., Grime, T., Guo, M., Morrison, J., 2012. A circulation model for the Discovery Islands, British Columbia. Atmos.-Ocean **50**, 301–316. http://dx.doi.org/10.1080/07055900.2012.686900.

Freeland, H.J., Farmer, D.M., 1980. Circulation and energetics of a deep, strongly stratified inlet. Can. J. Fish. Aquat. Sci. **37**, 1398–1410.

Henry, R.F., Walters, R.A., 1993. Geometrically based, automatic generator for irregular triangular networks. Commun. Numer. Methods Eng. **9**, 555–566.

Hunt, J.N., 1964. Tidal oscillations in Estuaries. Geophys. J. R. Astron. Soc. **8**, 440–455.

Mellor, G.L., Blumberg, A.F., 1985. Modeling vertical and horizontal diffusivities with the sigma coordinate system. Mon. Weather Rev. **113**, 1379–1383.

Mellor, G.L., Yamada, T., 1982. Development of a turbulence closure model for geophysical fluid problems. Rev. Geophys. 20 (4), 851–875.

Pietrzak, J., Jakobson, J.B., Burchard, H., Jacob Vested, H., Petersen, O., 2002. A three-dimensional hydrostatic model for coastal and ocean modelling using a generalised topography following co-ordinate system. Ocean Model. **4**, 173–205. http://dx.doi.org/10.1016/S1463-5003(01)00016-6.

Smagorinsky, J., 1963. General circulation experiments wiht the primitive equations I. The basic experiment. Mon. Weather Rev. **91**, 99–164. http://dx.doi.org/10.1126/science.27.693.594.

Stacey, M.W., 2005. Review of the partition of tidal energy in five Canadian fjords. J. Coast. Res. **21**, 731–746. http://dx.doi.org/10.2112/002-NIS.1.

Sverdrup, H.U., 1942. Prentice-Hall, New (Ed.), The Oceans Their Physics, Chemistry, and General Biology. Prentice-Hall, York, p. 1087, c1942 ed..

De Young, B., Pond, S., 1989. Partition of energy loss from the barotropic tide in fjords. J. Phys. Oceanogr. **19**, 246–252.